Sustained wet–dry cycling on early Mars

W. Rapin, G. Dromart, B. Clark, J. Schieber, E. Kite, L. Kah, L. Thompson, O. Gasnault, J. Lasue, P.-Y. Meslin, et al.

Manuscript accepted for Nature

Title (< 75 characters):

Sustained wet-dry cycling on early Mars

Authors:

W. Rapin[1]*, G. Dromart[2], B.C. Clark[3], J. Schieber[4], E.S. Kite[5], L.C. Kah[6], L.M. Thomson[7], O. Gasnault[1], J. Lasue[1], P-Y. Meslin[1], P.J. Gasda[8], N.L. Lanza[8]

Affiliations :

[1]Institut de Recherche en Astrophysique et Planétologie, Université de Toulouse 3 Paul Sabatier, CNRS, CNES; Toulouse, France.

[2]LGL-TPE, ENS de Lyon; Lyon, France.

[3]Space Science Institute, Littleton, CO, USA.

[4]Indiana University; Bloomington, IN, USA.

[5]University of Chicago; Chicago, IL, USA.

[6]University of Tennessee; Knoxville, TN, USA.

[7]University of New Brunswick; Fredericton, NB, Canada.

[8]Los Alamos National Laboratory; Los Alamos, NM, USA.

*Corresponding author. Email: william.rapin@irap.omp.eu

Summary paragraph (< 200 words):

The presence of perennially wet surface environments on early Mars is well-documented [1,2] but little is known about short-term episodicity in the early hydro-climate [3]. Post-depositional processes driven by such short-term fluctuations may produce distinct structures, yet are rarely preserved in the sedimentary record [4]. Incomplete geological constraints have led global models of the early Mars water cycle and climate to produce diverging results [5,6]. Here we report on new observations by the Curiosity rover at Gale crater indicating that high-frequency wet-dry cycling occurred in early Martian surface environments. We observe exhumed centimetric polygonal ridges with sulfate enrichments, joined at Y-junctions, that record cracks formed in fresh mud due to repeated wet-dry cycles of regular intensity. Instead of sporadic hydrological activity induced by impacts or volcanoes [5], our findings point to a sustained, cyclic, possibly seasonal, climate on early Mars. Further, as wet-dry cycling strongly promotes prebiotic polymerization [7,8], the Gale evaporitic basin may have been particularly conducive to these processes. The observed polygonal patterns are physically and temporally associated with the transition from smectite clays to sulfate-bearing strata, a globally distributed mineral transition [1]. This indicates that the Noachian-Hesperian transition (3.8 – 3.6 Gyrs ago) may have sustained an Earth-like climate regime and surface environments favourable to prebiotic evolution.

Main text:

Mars has a well-preserved sedimentary record that dates as far back as 4.3 Ga and perhaps earlier [9,10]. The early presence of habitable environments and even perennially wet surface environments has been well-established [1,2]. Little is known however about short-term episodicity and potential periodicity in early hydro-climate regimes [3]. Post-depositional processes driven by short-term fluctuations in a hydro-

climate regime mostly leave surficial imprints (e.g. mud cracks). Though prone to erosion, these are nonetheless critical for understanding past surface environments [4]. More generally, widely diverging models of the seasonality and episodicity of early Mars' water cycle and aridity are poorly constrained [11–16]. Here we report on well-preserved polygonal patterns exhumed from Hesperian-aged (~3.6 Gyrs old) strata that indicate wet-dry cycling and provide new insights on the hydro-climate and astrobiological potential of early Mars.

In situ investigation of hundreds of meters of sedimentary strata by the Mars Science Laboratory (MSL) Curiosity rover has documented ancient aqueous surface environments from fluvio-lacustrine [17] to more intermittent lake or lake margin settings [18,19]. After years of exploring strata dominated by smectite-bearing mudstones in the lower portion of the stratigraphic succession, the rover arrived at the sulfate-bearing unit, marking a major environmental transition [20] that is characteristic of stratified terrains across Mars [21]. Here, data collected by the rover have uncovered a new type of sulfate-enriched evaporitic-clastic deposit.

Pervasive centimeter scale polygonal patterns in the basal sulfate-bearing stratigraphic unit manifest as straight ridges that intersect with triple junctions. The most prominent occurrence was observed on the 3154th mission sol (Fig. 1 and Extended Data Fig. 1). Several additional occurrences were observed nearby within an 18 m elevation interval, and show comparable, as well as incipient and altered variants of these patterns (Extended Data Fig. 3). The polygons persist vertically to at least decimetric depth as shown by their stepped appearance on thick blocks of bedrock (Fig. 1b). On bedding planes, these polygons show ~1 cm relief, and an average diameter of about 4 cm (vary from 1 to 7 cm), with junction angles clustering at 120° (Extended Data Fig. 4). The ridges commonly consist of aligned nodules,

variably juxtaposed, and irregular in shape and size (Fig. 1d). Chemical composition documented by the ChemCam instrument shows a significant increase of Ca-sulfate and variable Mg-sulfate enrichment within the polygonal ridges and other nodular bedrock, whereas the smooth host bedrock in the polygon cores has basaltic bulk composition with sporadic Ca-sulfate detections but is dominantly sulfate-poor (Fig. 2 and Extended Data Table S2).

Although polygonal ridges in evaporitic settings on Earth can form as a consequence of subsurface salinity convection [22], we do not favor this interpretation here. Such terrestrial salt crusts are mostly pure and consist of ephemeral salt deposits that form larger polygons 0.5 to 2 m in size [23], and the lower gravity on Mars should have given rise to convection cells of even larger size than observed on Earth. Instead, we interpret the polygonal sulfate-bearing ridges as the fill of open desiccation cracks in muds by variably coalescent, salt-bearing and sediment-inclusive nodules (Fig. 3). Whereas desiccation cracks in fresh mud layers initially form T-junctions, maturation over repeated drying cycles results in hexagonal shapes with junction angles near 120°, i.e. Y-junctions [24]. In experiments, using clay layers, joint angles progressively tend towards 120° after 10 consecutive dryings with more cycles required to reach a homogeneous distribution centered at 120° and mature patterns of hexagonal shapes [25].

Abundant sulfates in the ridges and nodular bedrock (30 to 50 wt.% Ca-sulfate and up to 40 wt.% Mg-sulfate) and their much lower abundance in the host bedrock (Fig. 2) collectively suggest that sulfate minerals precipitated due to evaporation in muds and incorporated detrital sediment in the process. The present appearance of the sulfate-bearing ridges is likely not the original configuration of these features. More plausibly, they started out as evapoconcentration deposits focused on initially formed cracks that then evolved over a longer history of drying cycles and burial diagenesis (Fig. 3). They are now exposed

as erosion resistant polygonal ridges due to their higher degree of cementation relative to the host bedrock, and an early bias of surface salt precipitation in original mud-crack polygons (Fig. 3d).

Recurrent wetting of surface muds likely reflects a combination of flooding and groundwater recharge. Flooding could have dissolved salts that formed ephemeral surface crusts, as well as adding sediment and promoting burial, although air-fall is another possible sediment source. The length of surface cracks for a homogeneous medium scales to about 1.2 to 1.3 times its contraction depth [25]. Thus, the polygon size (a few centimeters, Fig. 1, Extended Data Fig. 4), implies desiccation and recharge events that only affected the uppermost few centimeters of the original muds. Deeper persistence of the polygonal pattern within bedrock (Fig. 1b) indicates upward propagation over the long term as the surface aggraded sediment (Fig 3). The distribution of junction angles well-centered at 120° and the absence of larger size lower-order polygons (Extended Data Fig. 4) suggests shallow depth repeated cycles of regular intensity. The variability in shape and size of the sulfate-rich nodules that precipitated within these cracks (now forming ridges) indicates multiple generations of nodule growth, congruous with significant intra-sediment salinity fluctuations due to repeated drying cycles.

Given the apparent repetition and limited desiccation depth, a few centimeters, wet-dry cycles could have been seasonal but potentially may also have occurred on shorter time scales. The time span over which these wet-dry cycles imprinted their signature is uncertain but may be estimated by considering the polygons' vertical distribution. Polygonal ridges are identified at multiple locations within an 18 m thick stratigraphic interval. Using floodplain and lake margin terrestrial analogs for sedimentation rate of 0.01 to 10 mm/yr[26–28], thousands to millions of years may be indicated by this sequence, with perhaps punctuated or spatially variable episodes of persistent wet-dry cycling. The polygonal pattern likely

propagated continuously through a stratigraphic interval > 2 m thick (Extended Data Fig. 4b) without depositional events producing visible horizons. This suggests that the sedimentation rate remained uniform and low enough for the pattern to propagate vertically with only thin clastic inputs during wettings, and without significant erosion during dryings (Fig. 3).

In summary, two key observations are (1) mature hexagonal shapes that indicates repeated drying cycles, and (2) their existence across stratigraphic thickness that implies that regular wet-dry conditions were maintained at least episodically in the long-term. Mud cracks were observed in underlying strata of the Murray formation, but these were predominantly T-junctions within a single horizon that suggest a single desiccation event [18,29]. The polygonal features reported here are therefore the first tangible evidence for sustained wet-dry cycling in early Martian surface environments, strengthening the case for regular episodicity in early Mars' hydrology on short timescales, likely seasonal or even shorter. This finding agrees with models [14,15] that rule out monotonically declining water supply in the aftermath of an asteroid impact or a single volcanic eruption to explain early fluvio-lacustrine activity [5], and instead favors a more sustained, Earth-like wet climate regime, with seasonal or shorter-term flooding. The presented evidence for sub-aerial desiccation in direct association with salt deposits also adds to the collective lines of evidence for evaporite deposition within the fluvio-lacustrine systems of early Mars [18,19]. While sulfates can form in ultra-cold climates [30], questioning the link between ancient sulfate salts and habitability on early Mars [31], our observations at Gale instead suggests surface temperatures associated with sulfate formation warm enough for liquid water.

In addition, environments subject to wet-dry cycling are considered supportive of, and perhaps essential, for prebiotic chemical evolution [7,8]. Due to desiccation, water activity is lowered and the concentration

of soluble ingredients in the residual liquid is increased, boosting reaction rates, especially for higher-order reactions [7]. For instance, the reactions that form nucleotides from their constituent nucleobases (ribose, phosphate) produce H_2O and hence are favored at low water activity. Most importantly, the polymerization reactions necessary to advance from nucleotides to RNA or DNA, and from amino acids to proteins, require dehydration steps which have been demonstrated to be facilitated by wet–dry cycles [32–34]. Also, dioctahedral smectites, i.e., swelling clays, similar to those present at Gale crater [35], and ubiquitous across Mars within environments interpreted as habitable [36], are capable of tightly adsorbing nucleotides through cation exchange on basal surfaces and have thus been proposed to help the concentration and polymerization of organics [37]. Under the right environmental conditions Darwin's proverbial "warm little pond" could significantly promote the reactions for macromolecule polymerization, and through sustained wet-dry cycling increase the likelihood of chemical evolution towards the origination of life [38].

In a broader regional context, there is widespread documentation of preserved organics in Gale crater sediments, containing up to ~0.5 kg/m^3, and a variety of other soluble elements [2]. The addition of direct evidence for a series of repeated wet-dry cycles presented here supports the conclusion that conditions in ancient Gale crater were conducive to prebiotic polymerization processes. There is also potential for wet-dry cycling to have occurred more broadly on Mars in the period when both intrabasin sulfate salts and smectite clays were deposited [1] as Gale is a stratigraphic section of global significance for this mineral assemblage near the Noachian-Hesperian transition [20,39] (Fig. 4). Some of these globally distributed strata may thus harbor well-preserved evidence of prebiotic chemical evolution, a record that is no longer available on Earth [40]. On the basis of this new evidence for wet-dry cycling within surface environments, and considering the delivery of organics and accumulation of volatiles on the Martian

surface for almost a billion years prior (Fig. 4), our findings suggest that the Noachian-Hesperian transition period could have been favourable for the emergence of life; possibly more so than the earlier Noachian eon with its potential for perennially wet surface environments [21].

Main references:

1. Ehlmann, B. L. & Edwards, C. S. Mineralogy of the Martian Surface. *Annu. Rev. Earth Planet. Sci.* **42**, 291–315 (2014).
2. Vasavada, A. R. Mission Overview and Scientific Contributions from the Mars Science Laboratory Curiosity Rover After Eight Years of Surface Operations. *Space Sci. Rev.* **218**, 1–65 (2022).
3. Kite, E. S. Geologic Constraints on Early Mars Climate. *Space Sci. Rev.* **215**, 10 (2019).
4. Sheldon, N. D. & Tabor, N. J. Quantitative paleoenvironmental and paleoclimatic reconstruction using paleosols. *Earth-Sci. Rev.* **95**, 1–52 (2009).
5. Wordsworth, R. The Climate of Early Mars. *Annu. Rev. Earth Planet. Sci.* **44**, 381–408 (2016).
6. Ramirez, R. M. & Craddock, R. A. The geological and climatological case for a warmer and wetter early Mars. *Nat. Geosci.* **11**, 230–237 (2018).
7. Campbell, T. D. *et al.* Prebiotic condensation through wet–dry cycling regulated by deliquescence. *Nat. Commun.* **10**, 4508 (2019).
8. Becker, S. *et al.* Wet-dry cycles enable the parallel origin of canonical and non-canonical nucleosides by continuous synthesis. *Nat. Commun.* **9**, 163 (2018).
9. Farley, K. A. *et al.* In Situ Radiometric and Exposure Age Dating of the Martian Surface. *Science* **343**, 1247166 (2014).
10. Goodwin, A., Garwood, R. J. & Tartèse, R. A Review of the "Black Beauty" Martian Regolith Breccia and Its Martian Habitability Record. *Astrobiology* **22**, 755–767 (2022).

11. Guzewich, S. D. *et al.* 3D Simulations of the Early Martian Hydrological Cycle Mediated by a H2-CO2 Greenhouse. *J. Geophys. Res. Planets* **126**, e2021JE006825 (2021).
12. Kamada, A., Kuroda, T., Kasaba, Y., Terada, N. & Nakagawa, H. Global climate and river transport simulations of early Mars around the Noachian and Hesperian boundary. *Icarus* **368**, 114618 (2021).
13. Kite, E. S., Steele, L. J., Mischna, M. A. & Richardson, M. I. Warm early Mars surface enabled by high-altitude water ice clouds. *Proc. Natl. Acad. Sci.* **118**, e2101959118 (2021).
14. Turbet, M. & Forget, F. 3-D Global modelling of the early martian climate under a dense CO2+ H2 atmosphere and for a wide range of surface water inventories. *ArXiv Prepr. ArXiv210310301* (2021).
15. Steakley, K., Murphy, J., Kahre, M., Haberle, R. & Kling, A. Testing the impact heating hypothesis for early Mars with a 3-D global climate model. *Icarus* **330**, 169–188 (2019).
16. Stucky de Quay, G., Goudge, T. A., Kite, E. S., Fassett, C. I. & Guzewich, S. D. Limits on Runoff Episode Duration for Early Mars: Integrating Lake Hydrology and Climate Models. *Geophys. Res. Lett.* **48**, e2021GL093523 (2021).
17. Grotzinger, J. P. *et al.* Deposition, exhumation, and paleoclimate of an ancient lake deposit, Gale crater, Mars. *Science* **350**, aac7575 (2015).
18. Rapin, W. *et al.* An interval of high salinity in ancient Gale crater lake on Mars. *Nat. Geosci.* **12**, 889–895 (2019).
19. Schieber, J. *et al.* Mars is a mirror – Understanding the Pahrump Hills mudstones from a perspective of Earth analogues. *Sedimentology* **69**, 2371–2435 (2022).
20. Milliken, R. E., Grotzinger, J. P. & Thomson, B. J. Paleoclimate of Mars as captured by the stratigraphic record in Gale Crater. *Geophys. Res. Lett.* **37**, L04201 (2010).
21. Bibring, J.-P. *et al.* Global Mineralogical and Aqueous Mars History Derived from OMEGA/Mars Express Data. *Science* **312**, 400–404 (2006).

22. Lasser, J., Nield, J. M. & Goehring, L. Surface and subsurface characterisation of salt pans expressing polygonal patterns. *Earth Syst. Sci. Data* **12**, 2881–2898 (2020).
23. Goodall, T. M., North, C. P. & Glennie, K. W. Surface and subsurface sedimentary structures produced by salt crusts. *Sedimentology* **47**, 99–118 (2000).
24. Goehring, L., Conroy, R., Akhter, A., J. Clegg, W. & F. Routh, A. Evolution of mud-crack patterns during repeated drying cycles. *Soft Matter* **6**, 3562–3567 (2010).
25. Goehring, L. Evolving fracture patterns: columnar joints, mud cracks and polygonal terrain. *Philos. Trans. R. Soc. Math. Phys. Eng. Sci.* **371**, 20120353 (2013).
26. Sadler, P. M. Sediment Accumulation Rates and the Completeness of Stratigraphic Sections. *J. Geol.* **89**, 569–584 (1981).
27. Daniels, J. M. Floodplain aggradation and pedogenesis in a semiarid environment. *Geomorphology* **56**, 225–242 (2003).
28. Kraus, M. J. Paleosols in clastic sedimentary rocks: their geologic applications. *Earth-Sci. Rev.* **47**, 41–70 (1999).
29. Stein, N. *et al.* Desiccation cracks provide evidence of lake drying on Mars, Sutton Island member, Murray formation, Gale Crater. *Geology* **46**, 515–518 (2018).
30. Baccolo, G. *et al.* Jarosite formation in deep Antarctic ice provides a window into acidic, water-limited weathering on Mars. *Nat. Commun.* **12**, 436 (2021).
31. Niles, P. B. & Michalski, J. Meridiani Planum sediments on Mars formed through weathering in massive ice deposits. *Nat. Geosci.* **2**, 215–220 (2009).
32. Becker, S. *et al.* Unified prebiotically plausible synthesis of pyrimidine and purine RNA ribonucleotides. *Science* **366**, 76–82 (2019).

33. Higgs, P. G. The Effect of Limited Diffusion and Wet-Dry Cycling on Reversible Polymerization Reactions: Implications for Prebiotic Synthesis of Nucleic Acids. *Life* **6**, E24 (2016).
34. Ross, D. S. & Deamer, D. Dry/Wet Cycling and the Thermodynamics and Kinetics of Prebiotic Polymer Synthesis. *Life* **6**, 28 (2016).
35. Bristow, T. F. *et al.* Clay mineral diversity and abundance in sedimentary rocks of Gale crater, Mars. *Sci. Adv.* **4**, eaar3330 (2018).
36. Bishop, J. L. *et al.* What the ancient phyllosilicates at Mawrth Vallis can tell us about possible habitability on early Mars. *Planet. Space Sci.* **86**, 130–149 (2013).
37. Pedreira-Segade, U., Feuillie, C., Pelletier, M., Michot, L. J. & Daniel, I. Adsorption of nucleotides onto ferromagnesian phyllosilicates: Significance for the origin of life. *Geochim. Cosmochim. Acta* **176**, 81–95 (2016).
38. Clark, B. C. & Kolb, V. M. Macrobiont: Cradle for the Origin of Life and Creation of a Biosphere. *Life* **10**, 278 (2020).
39. Grotzinger, J. P. & Milliken, R. E. The Sedimentary Rock Record of Mars: Distribution, Origins, and Global Stratigraphy. in *Sedimentary Geology of Mars* (eds. Grotzinger, J. P. & Milliken, R. E.) vol. 102 0 (SEPM Society for Sedimentary Geology, 2012).
40. Knoll, A. H. Paleobiological Perspectives on Early Microbial Evolution. *Cold Spring Harb. Perspect. Biol.* **7**, a018093 (2015).
41. Thomson, B. J. *et al.* Constraints on the origin and evolution of the layered mound in Gale Crater, Mars using Mars Reconnaissance Orbiter data. *Icarus* **214**, 413–432 (2011).
42. Le Deit, L. *et al.* Sequence of infilling events in Gale Crater, Mars: Results from morphology, stratigraphy, and mineralogy. *J. Geophys. Res. Planets* **118**, 2439–2473 (2013).

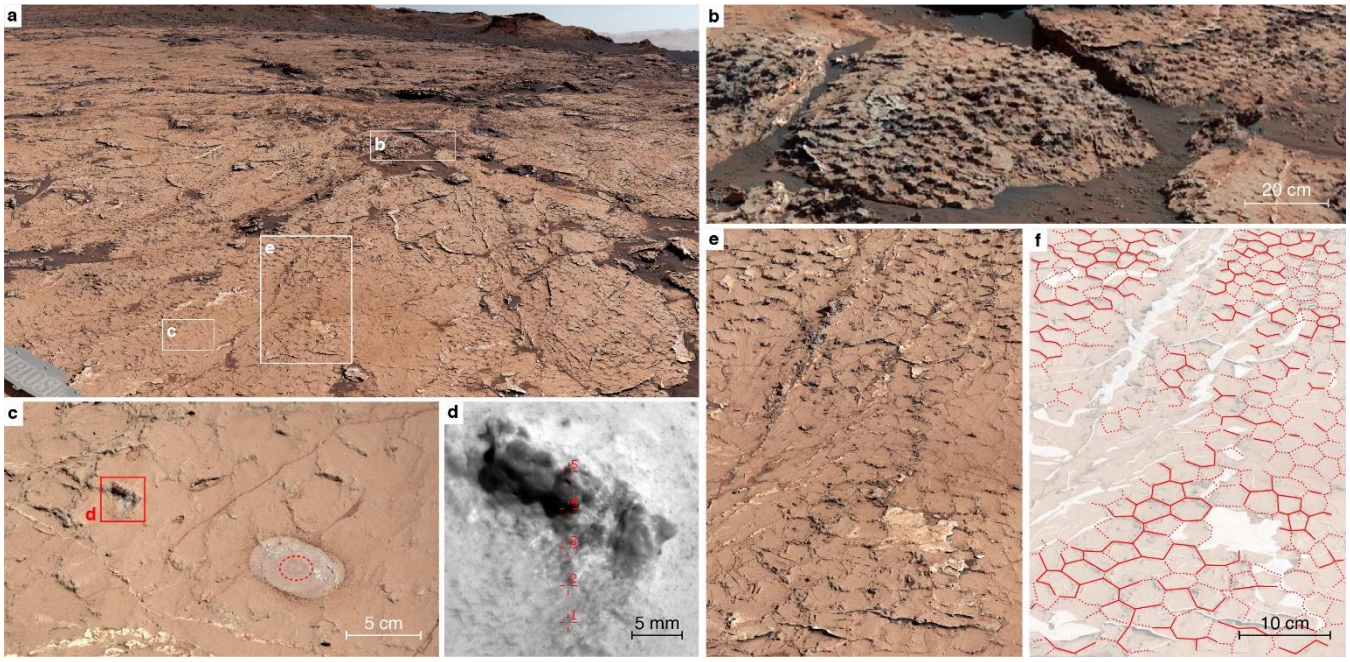

Fig. 1: Polygonal ridges - *in situ* observations. **a**, General view of bedrock surrounding the rover on sols 3154 to 3156 showing widespread polygonal ridges (mcam100270; larger image Extended Data Fig. 2). **b**, Close-up showing "stepped" exposure of polygons within large bedrock blocks. **c**, View of bedrock (mcam100287) with polygons and locations of ChemCam analysis on ridge (red rectangle) and APXS analysis on smooth host bedrock (dotted circle). **d**, Remote micro-image of cemented ridge with spots analyzed by ChemCam (reticles 1 to 5), highlighting details of nodular texture (ccam01156). **e**, Bedrock with polygonal pattern and interpretative overlay (**f**) that shows prominent ridges (solid red lines), less certain ridges (dotted red lines), and crosscutting later stage Ca-sulfate filled veins (white areas) (mcam100276).

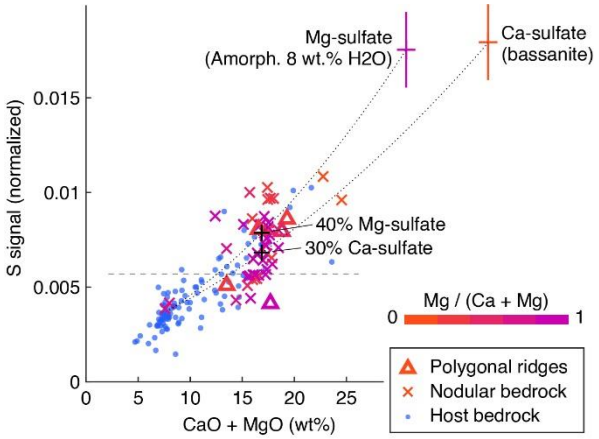

Fig. 2: Bedrock enrichments in Ca/Mg-sulfate. ChemCam sulfur signal as a function of CaO and MgO for smooth host bedrock (blue) and nodular bedrock including polygonal ridges (red-purple). Dotted line corresponds to mixing of sulfates with average siliciclastic host bedrock ; end-members are shown by black crosses and blue cross indicate host bedrock mean composition. The sulfur signal limit of detection at SO_3 > 10.6 wt.% is also shown (horizontal dashed line). Vertical error bars on end-members represent sulfate content calibration uncertainty.

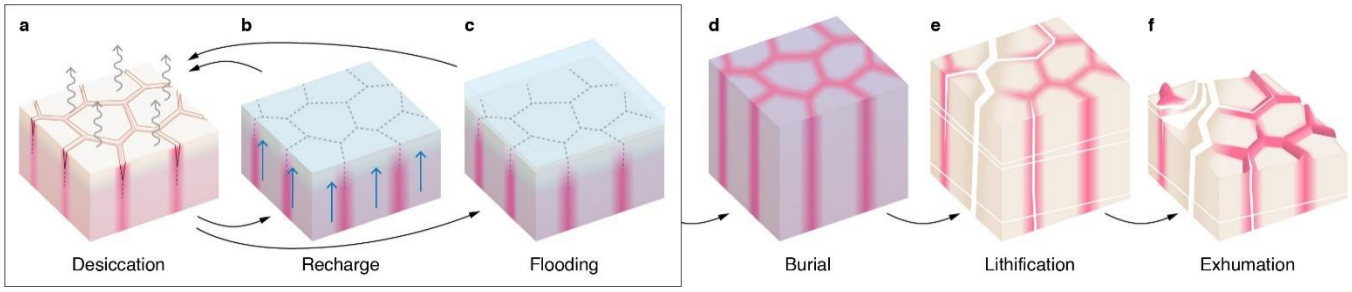

Fig. 3: Formation model for sulfate-enriched polygonal ridges. Repeated cycles of desiccation (**a**), recharge (**b**) and flooding (**b**) form a vertically propagating hexagonal pattern of sulfate enrichment. **a**, Evaporation desiccates and cracks near-surface sediment, triggering salt crystallization (red) at and near cracks where the subsurface brine (purple) concentrates. **b**, Water recharge heals cracks by sediment hydration. **c**, Flooding dissolves excess salts at the surface but subsurface brine and intrasediment sulfate salts are preserved and siliciclastic sediment is deposited on top. **d**, Sediment is buried with saturated brine in pore spaces and sulfates are mostly preserved. **e**, Later diagenesis partially dissolves intra-sediment sulfate salts and late diagenetic fractures are filled with Ca-sulfate (white). **f**, Sulfate-cemented polygonal ridges become visible during exhumation as the softer host bedrock is preferentially removed during weathering.

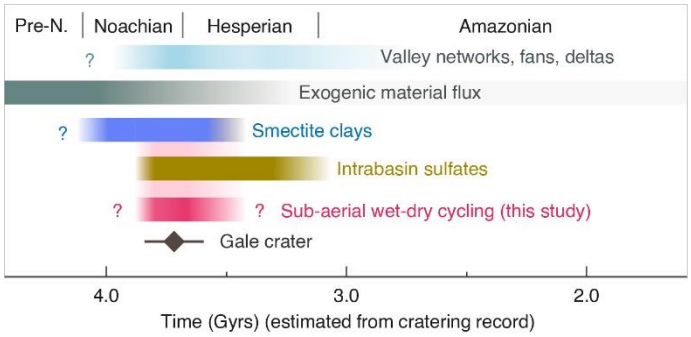

Fig. 4: Mars' potential for prebiotic record. Evidence for sub-aerial wet-dry cycling could be relevant to the early Noachian-Hesperian transition period during which both intrabasin sulfates and smectite clays formed [1]. Timing for Gale impact (diamond) with uncertainty covers the different reported ages [41,42]. Exogenic material flux is a proxy for the delivery of organics to the surface (Extended Data Fig. 5). Timing for valley networks, fans and deltas derived from crater counting on geomorphic features [3].

Methods

Rover-based geochemical datasets and data processing. The Curiosity rover has 5 instruments that can measure geochemistry and mineralogy [43]. Thus, ChemCam is the primary source of available chemical data. ChemCam is a laser-induced breakdown spectrometer (LIBS) that provides chemical analyses at a submillimeter scale and detailed images with the Remote Micro Imager (RMI) [44,45]. Major-element contents were obtained using the current calibration model [46]. Water and sulfate contents were estimated using dedicated calibration models : for water content quantification uses the hydrogen signal [47], and for sulfate content the sulfur signal is used with in situ calibration as previously described for sulfate enrichments observed elsewhere in the Murray formation [18]. Although the arm-mounted APXS instrument did not sample polygonal ridges owing to operational constraints, it provided a bulk (~2 cm diameter area) measurement on brushed, smoothed host bedrock immediately adjacent to a raised, resistant ridge (Fig. 1c) highlighting the absence of sulfate enrichment (Extended Data Table S2). APXS data from other bedrock targets and resistant features in the vicinity of the polygonal features also support the concentration of Mg- and Ca-sulfates in the resistant features (Extended Data Fig. 6). CheMin and SAM analyses (which provide mineralogy and evolved gas analysis respectively from powdered, drilled sample) were not acquired on the polygonal ridges and most of the nodular bedrock.

Identification of the nodular lithology. The nodular lithology was identified based on images using both MastCam and ChemCam RMI. The lithology is characterized by protruding, erosion-resistant forms of near centimeter-scale connected to the host bedrock. They are variably shaped, widespread and abundant in the examined section (Extended Data Fig. 3). The ChemCam RMI was used to associate point by point the LIBS measurements with either smooth host bedrock (e.g. Extended Data Fig. 7) or nodular bedrock (e.g. Extended Data Fig. 8). This careful classification of all ChemCam data acquired within the examined section provides exhaustive geochemical data from the bedrock, removing points

with soil contribution or bad laser focus. The full list of points classified from either host or nodular is shown on Extended Data Table S3.

Lithology of sulfate-bearing nodular bedrock. Nodules are widespread, highly variable in density in the examined section (Extended Data Fig 3), and occur as three morphologic types: rounded, dendritic, and vacuolar. Rounded forms are up to 1 cm in diameter and more resistant to erosion than the host bedrock. Nodules can be spherical to sub-spherical, and can show variable clustering and coalescence to form incipient to well-developed nodular ridges (Extended Data Fig. 9a,b). Dendritic nodules are jagged, multifaceted, multi-centimeter forms that are evenly distributed on bedding planes at certain intervals, and resemble rosette-like aggregates (Extended Data Fig. 7a,b,d). The vacuolar nodules are large (up to decimeter scale), polymorphic forms which apparently resulted from random amalgamation of nodules. Their coalescence is partial. Now visible voids likely represent spots once occupied by uncemented host bedrock that has been removed by eolian erosion processes [48]. Vacuolar nodules are pervasive at the top of the studied interval (Extended Data Fig. 11). Outcrops with laminae consisting of variably coalescent micro-nodules were also observed within the section, although not analyzed by the rover chemical instruments (Extended Data Fig. 9e).

Polygonal Pattern Analysis. To generate the map over which the polygonal pattern was analyzed (Extended Data Fig. 4a), we used the Onsight software (https://software.nasa.gov/software/NPO-50830-1) which was developed by the Jet Propulsion Laboratory for the context of Mars exploration. Onsight renders a three-dimensional reconstruction and visualization of the surface of Mars from a variety of images. For our purpose, it allowed orthoprojection to the surface, with orthoprojected scale, of the Mastcam mosaics. Most of the polygon morphologies are hexagonal, and resemble honeycomb or hexagon floor tiles. Pentagonal forms are common. Rare quadrangle and heptagonal patterns have also been observed.

The size of the polygons is approximated by the diameter of the circles that are enclosed within the polygons, i.e. circles that are tangential to polygon sides. The circles were manually drawn, and diameter of the individual polygons was measured using Adobe Illustrator® software applied to the Onsight orthoprojection of the mosaics acquired on sols 3152 - 3154 (West Section) (Extended Data Fig. 4a). The polygons that were selected for analysis are those that offer a fairly regular shape, i.e. the polygons that have equal to subequal side lengths. The unmarked areas are those for which late diagenetic veins intersect and disturb the original polygonal ridge pattern, and those for which the original polygonal ridges have been stripped off after exhumation by dissolution and/or deflation.

The average diameter of the 467 circles that were analyzed by a single operator over a surface of about 3.75 square meters is 3.9 cm, with the smallest and largest specimen at 1.73 cm and 7.56 cm, respectively (Extended Data Table S1). To have a notion of the degree of precision of our method, a second operator made a test by repeating the marking and measurements over Block 1 (Extended Data Fig. 4a). The test revealed that: (i) the number of polygons distinguished by the operators is minimal, i.e. 168 against 176; (ii) mean size varies from 3.43 to 3.98 cm, which is a relative error of only ~16%, at best.

The frequency distribution of diameter cm values shows an unimodal asymmetrical, i.e. Poisson probability distribution (Extended Data Fig. 4c). Distinct blocks of similar areas yield similar polygonal pattern's characteristics (Extended Data Table S1), which suggests the polygon-bearing bedrock originally was homogeneous in terms of texture (porosity; grain-size) and mineralogical composition, laterally at multi-metric scale.

The junction angles were measured on the Onsight orthoprojection within a larger area to extend the number of samples. Junctions and ridges between junctions were mapped using QGIS software from which angles were computed. For a junction with only two connected ridges mapped, only one angle is measured. For triple junctions, with three connected ridges identified, the 3 angles are computed forming

a total of 360°. Well-expressed and clearly identified ridges are differentiated from ridges with more altered and uncertain for test, with a total 2214 angles identified total, 532 of them classified as angles only for well-expressed ridges. The frequency distributions show a similar modal angle near 120°, then a gaussian fit was performed on all identified angles and found centered at 119.1° (Extended Data Fig. 4c).

Methods references:

43. Grotzinger, J. P. *et al.* Mars Science Laboratory Mission and Science Investigation. *Space Sci. Rev.* **170**, 5–56 (2012).
44. Maurice, S. *et al.* The ChemCam Instrument Suite on the Mars Science Laboratory (MSL) Rover: Science Objectives and Mast Unit Description. *Space Sci. Rev.* **170**, 95–166 (2012).
45. Wiens, R. C. *et al.* The ChemCam Instrument Suite on the Mars Science Laboratory (MSL) Rover: Body Unit and Combined System Tests. *Space Sci. Rev.* **170**, 167–227 (2012).
46. Clegg, S. M. *et al.* Recalibration of the Mars Science Laboratory ChemCam instrument with an expanded geochemical database. *Spectrochim. Acta Part B At. Spectrosc.* **129**, 64–85 (2017).
47. Rapin, W. *et al.* Quantification of water content by laser induced breakdown spectroscopy on Mars. *Spectrochim. Acta Part B At. Spectrosc.* **130**, 82–100 (2017).
48. Schieber, J. *et al.* Engraved on the rocks—Aeolian abrasion of Martian mudstone exposures and their relationship to modern wind patterns in Gale Crater, Mars. *Depositional Rec.* **6**, 625–647 (2020).
49. Hartmann, W. K. & Neukum, G. Cratering Chronology and the Evolution of Mars. *Space Sci. Rev.* **96**, 165–194 (2001).
50. Quantin-Nataf, C., Craddock, R. A., Dubuffet, F., Lozac'h, L. & Martinot, M. Decline of crater obliteration rates during early martian history. *Icarus* **317**, 427–433 (2019).

Acknowledgments:
Thanks to A. Vasavada and A. Fraeman for discussions that helped improve this work. The authors would like to thank T. Goudge and J. Bishop for the constructive comments and review of this work. Data used are available in the NASA Planetary Data System Geoscience Node in the MSL directory (https://pds-geosciences.wustl.edu/missions/msl/). This project was supported in the USA by NASA's Mars Exploration Program and in France is conducted under the authority of CNES. Mastcam mosaics were processed by the Mastcam team at Malin Space Science Systems. Edwin Kite funding by NASA grant 80NSSC22K0731. Lucy Thompson funding as MSL team member is provided by the CSA.

Author contributions:
W.R. and G.D. equally led the writing of the manuscript. W.R., G.D., B.C.C., J.S., L.C.K., L.M.T., P.J.G., P.Y.M. and J.L. contributed to methodology, investigation and data processing. O.G. and N.L.L. are the leads of the ChemCam instrument investigation. J.S. and E.S.K. provided significant contributions to the writing and reviewing of the manuscript. All co-authors provided helpful comments and inputs to the manuscript.

Competing interests: Authors declare no competing interests.

Data and materials availability: All data are available in in the NASA Planetary Data System (https://pds.nasa.gov/) or the supplementary information.

Supplementary Information is available for this paper.

Correspondence and requests for materials should be addressed to W.R.

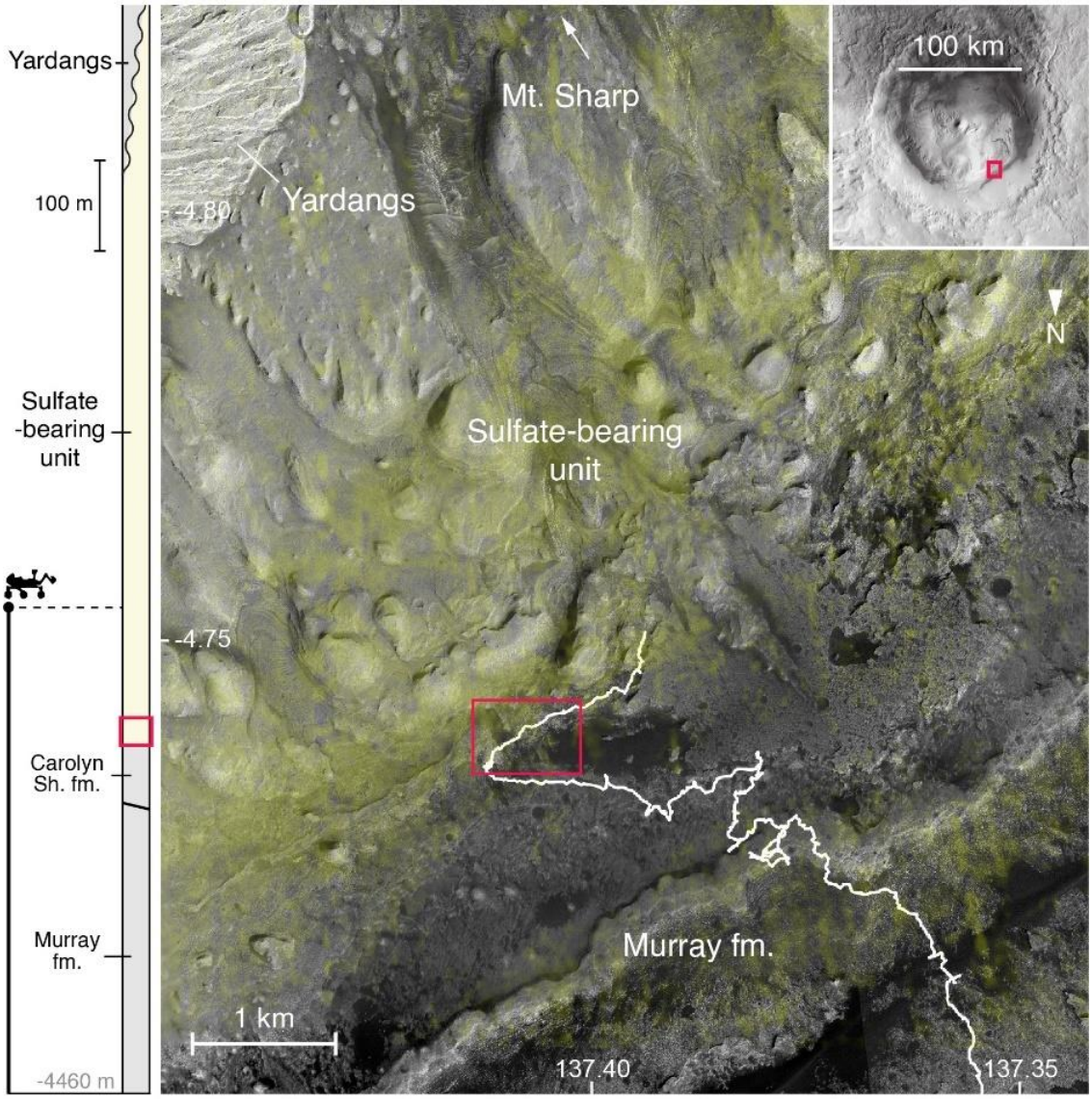

Extended Data Fig. 1: Context of observations in Gale crater, Mars. Stratigraphic context (left) of the lower portion of Mount Sharp and map (right) showing Curiosity rover traverse (white) on the High Resolution Imaging Science Experiment (HiRISE) base map overlaid with Compact Reconnaissance Imaging Spectrometer for Mars (CRISM) S-index, which tracks sulfates (shaded yellow). Red rectangle shows the location of close-up map and detailed stratigraphy (Extended Data Fig. 3b).

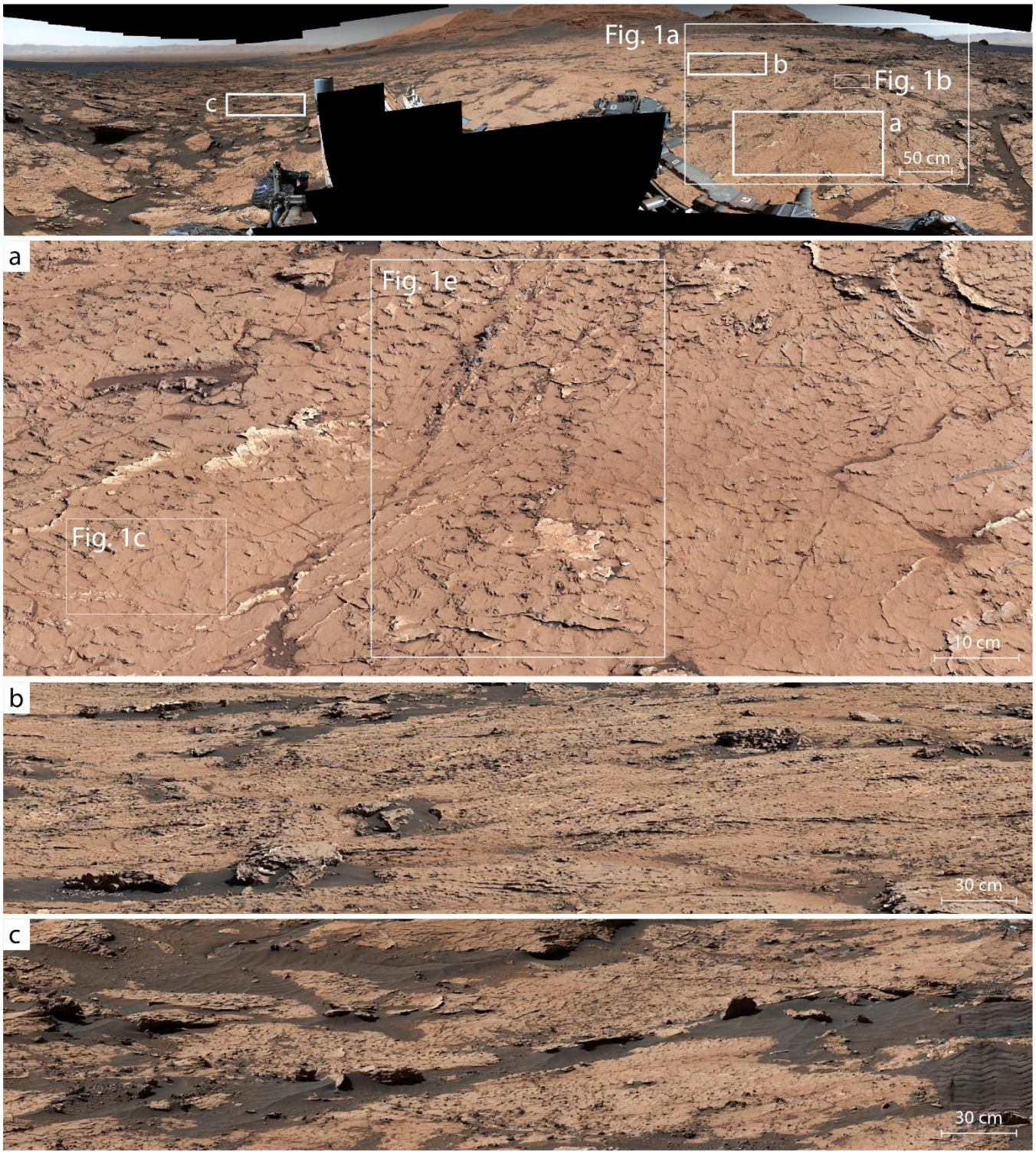

Extended Data Fig. 2: Larger color image of bedrock with polygonal ridges for context. MastCam image (mcam100270) and close-ups (**a**, **b** and **c**) with rectangle locations of close-up view from Fig. 1. Close-ups (**b**, **c**) show bedrock 10 to 20 meters away where regularly spaced ridges and nodules can be observed supporting lateral extension of the same polygonal pattern although camera resolution prevents detailed geometrical analysis at this distance.

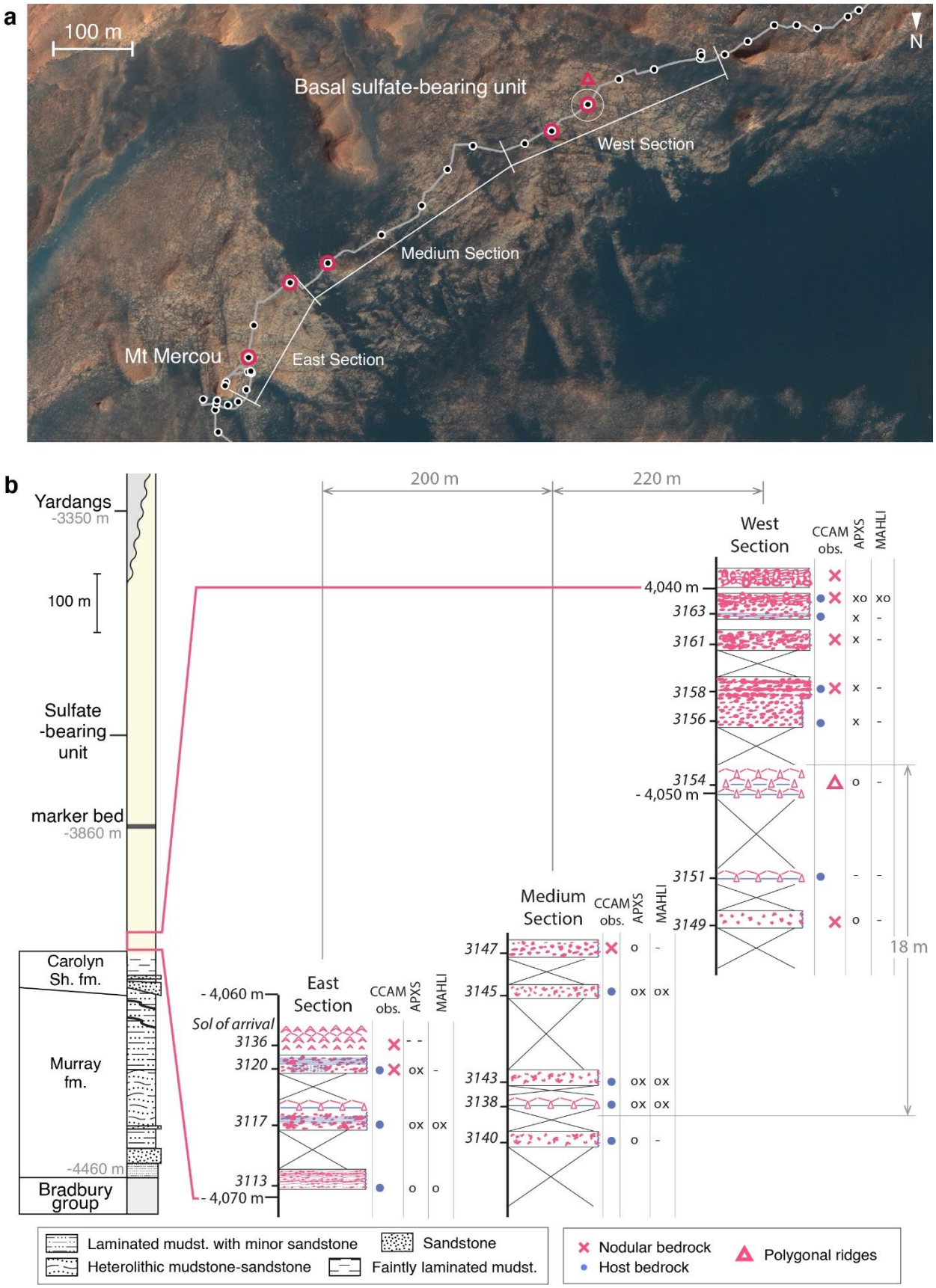
a
100 m
N
Basal sulfate-bearing unit
West Section
Medium Section
East Section
Mt Mercou
b
200 m
220 m
Yardangs
-3350 m
100 m
Sulfate
-bearing
unit
marker bed
-3860 m
Carolyn
Sh. fm.
Murray
fm.
-4460 m
Bradbury
group
West
Section
CCAM
obs.
APXS
MAHLI
4,040 m
3163
3161
3158
3156
3154
- 4,050 m
3151
3149
18 m
Medium
Section
3147
3145
3143
3138
3140
East
Section
- 4,060 m
Sol of arrival
3136
3120
3117
3113
- 4,070 m
Laminated mudst. with minor sandstone
Heterolithic mudstone-sandstone
Sandstone
Faintly laminated mudst.
Nodular bedrock
Host bedrock
Polygonal ridges

Extended Data Fig. 3: Local stratigraphic context of the examined section. Close-up map of the examined sections along the rover traverse with location of the observed polygonal pattern (red circles) and associated geochemical measurements (red triangle and diamond, see Fig. 2, 3) (**a**); as well as general stratigraphic column for context with detailed log facies for East (Extended Data Fig. 9), Medium (Extended Data Fig. 10), and West (Extended Data Fig. 11) sections (**b**). Other locations with possible polygonal ridges as incipient or altered variants are annotated in Extended Data Fig. 12. The approximate distance of 200 m and 220 m between the adjacent sections centers is annotated on top (**b**). Facies are drawn based on available images from Mastcam M34/M100, MAHLI and ChemCam RMI. Nodular features within bedrock interpreted as chemical deposits are highlighted in red, whereas physical sedimentary structures are shown in blue. Sedimentary structures were rarely observed and the host rock of chemical deposits was mostly smooth and featureless. Geochemical data from polygonal ridges are represented with triangle (**a** and **b**). Location of ChemCam LIBS observations on bedrock are shown in the "CCAM obs." column with a red cross where points analyzed chemical deposits and blue dot for host rock. Locations of APXS and MAHLI observations are also highlighted the same way, with a cross for chemical deposits and circle for host bedrock.

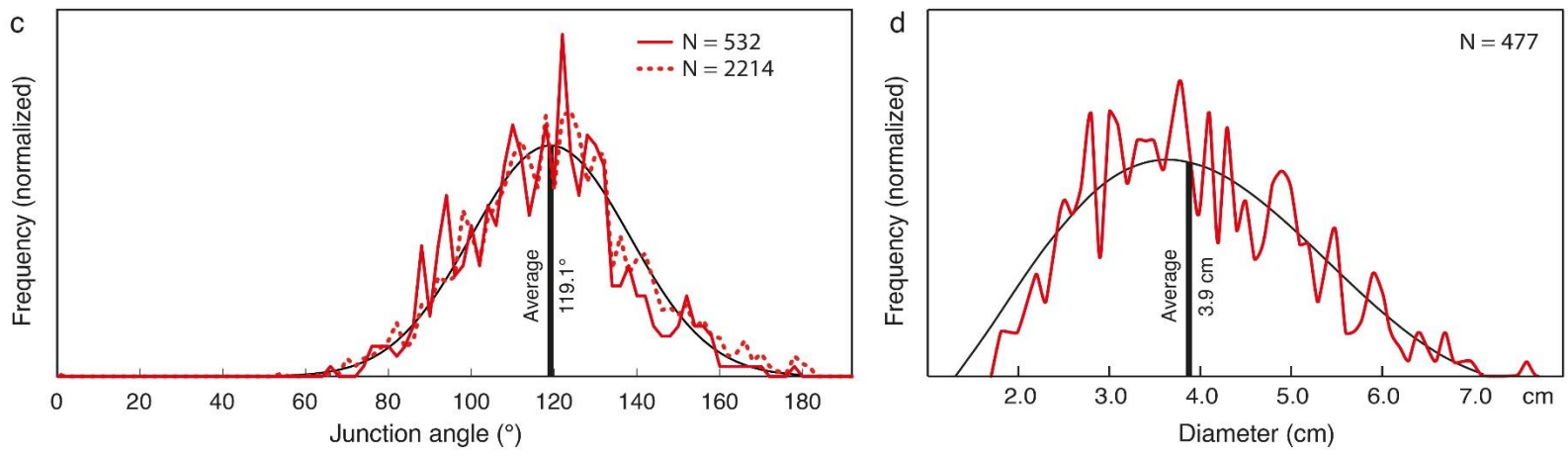

Extended Data Fig. 4: Polygonal ridges pattern analysis. Top view of bedrock from sol 3154 generated using Onsight, with circles representing marked polygon sizes (blue) and junctions (yellow dots) connected to well-expressed (solid lines) and uncertain ridges (dashed lines) forming the pattern mapped on image (**a**). Red contour represents the area covered on Fig. 1e, and white rectangles areas for polygon size statistics (Extended Data Table 1). Top view with extended context shows the area of analysis along with the location of closeups where polygonal ridges are observed in the distance (**b**). Elevation change is indicated by 1 m contour lines (yellow) to estimate the thickness of the observable strata from this location. Distribution of junction angles for well-expressed ridges only (solid red) and all ridges (dashed red) with gaussian fit (**c**). Distribution of polygon sizes and fit with Poisson probability distribution (**d**), see Extended Data Table 1.

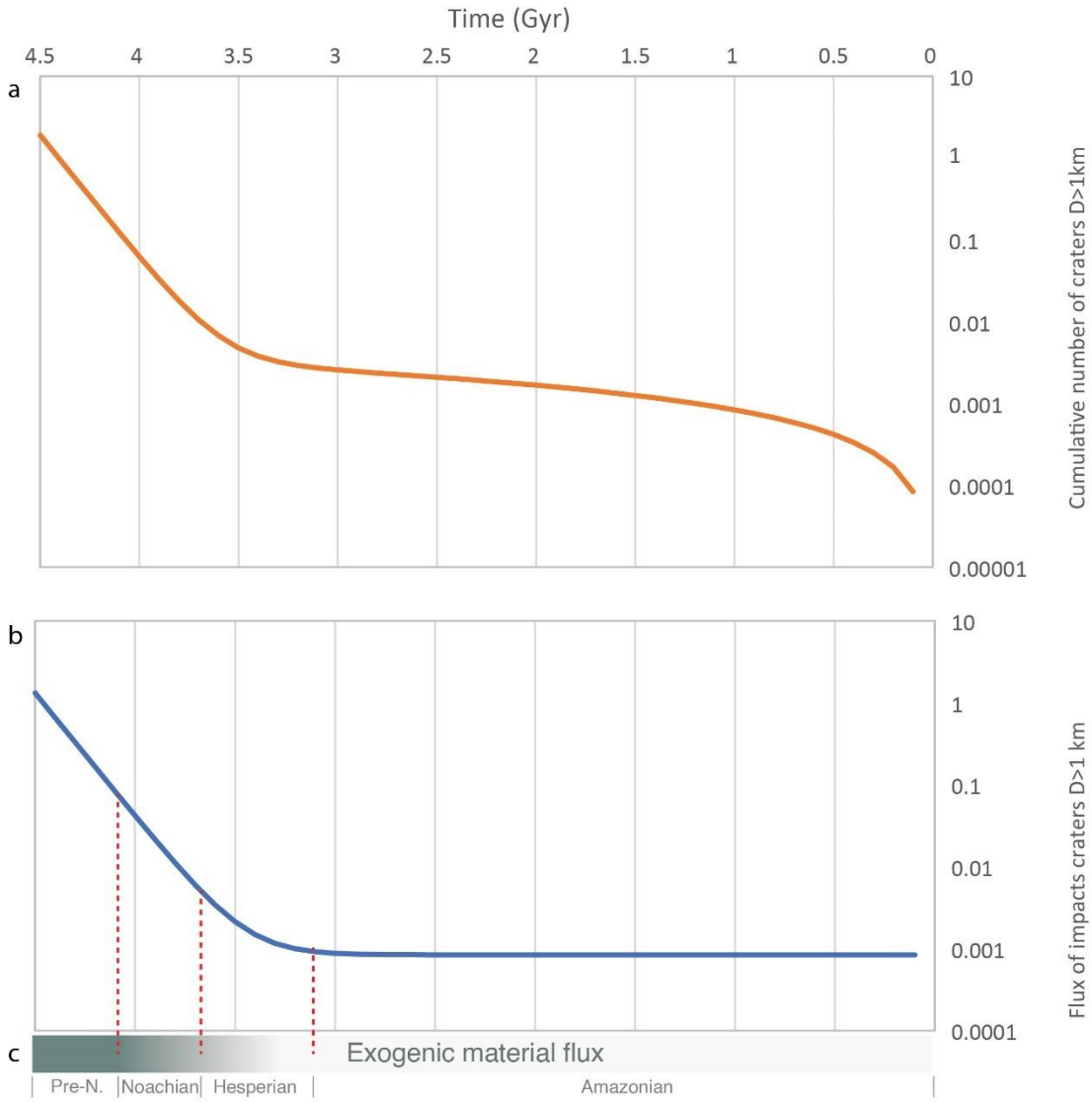

Extended Data Fig. 5: Flux of impacts on Mars through time. Curves representing the impact rate chronology on Mars based on cumulative density of craters with D>1 km per unit area (**a**). This model is based on the equation from the crater chronology [49,50] giving the cumulative number of craters larger than 1 km as $N(1) = 5.44\times10^{-14}[\exp(6.93\ T) - 1] + 8.38\times 10^{-4}\ T$. The derivative of this function gives the flux of impact craters larger than 1 km over time (**b**) is given by the equation: $N'(1) = 3.77\times10^{-13}[\exp(6.93\ T) - 1] + 8.38\times 10^{-4}\ T$. This curve presents a strong decrease in intensity of cratering with time which can be used as a proxy for extra-terrestrial material accretion with time. The link between the flux of impact craters of a given size and the accretion flux of the planet is then shown as a gradient bar (**c**) that is represented on Fig. 4 in the main text.

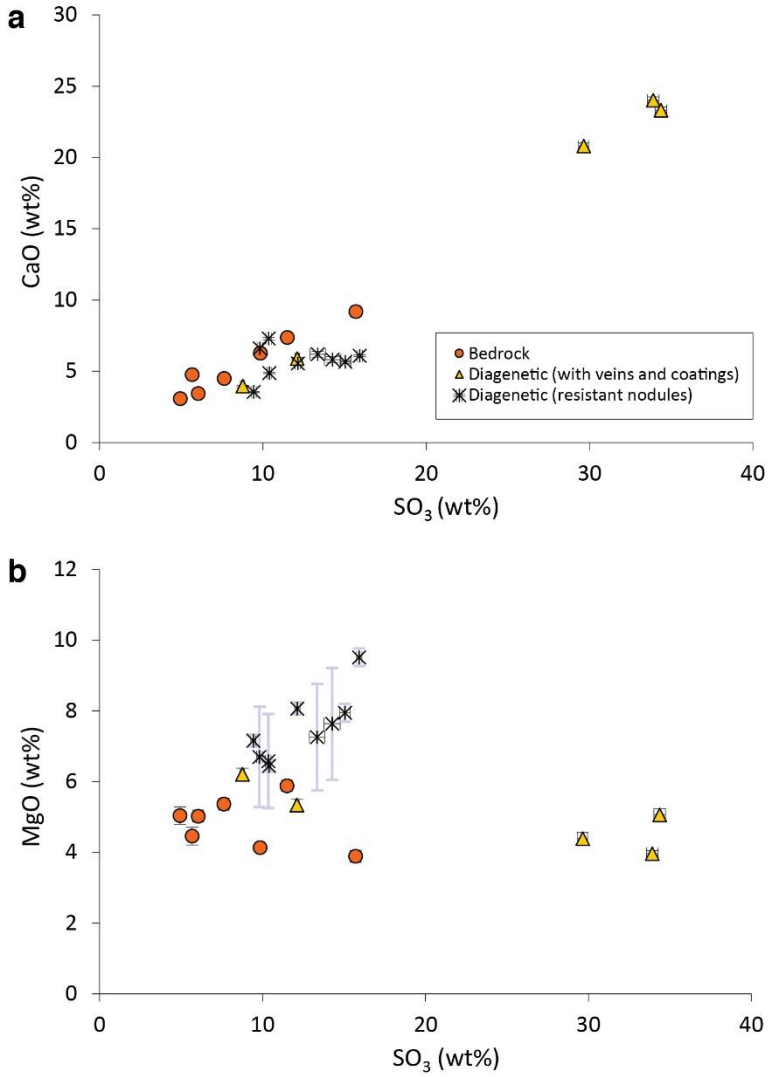

Extended Data Fig. 6: APXS data bedrock and diagenetic features. CaO (**a**) and MgO (**b**) versus SO_3 content for bedrock and diagenetic features in the investigated section. Resistant nodules, forming collectively nodular bedrock, show MgO and SO3 enrichment. The data only includes relatively clean, dust-free targets. List of target names for bedrock: Gourdon, Bardou_DRT, Ribagnac_DRT, Chenaud_DRT, Monpazier, Plaisance_DRT, Monsec_DRT. For veins/coating: Terrasson_Lavilledieu, Festalemps_DRT, Quinsac, Biras, Pezuls. For resistant bedrock: Gardonne_DRT, Simeyrols, Rouffignac, Bosset, Bosset_offset, Nabirat, Sarlande, Salagnac, Le_Bugue.

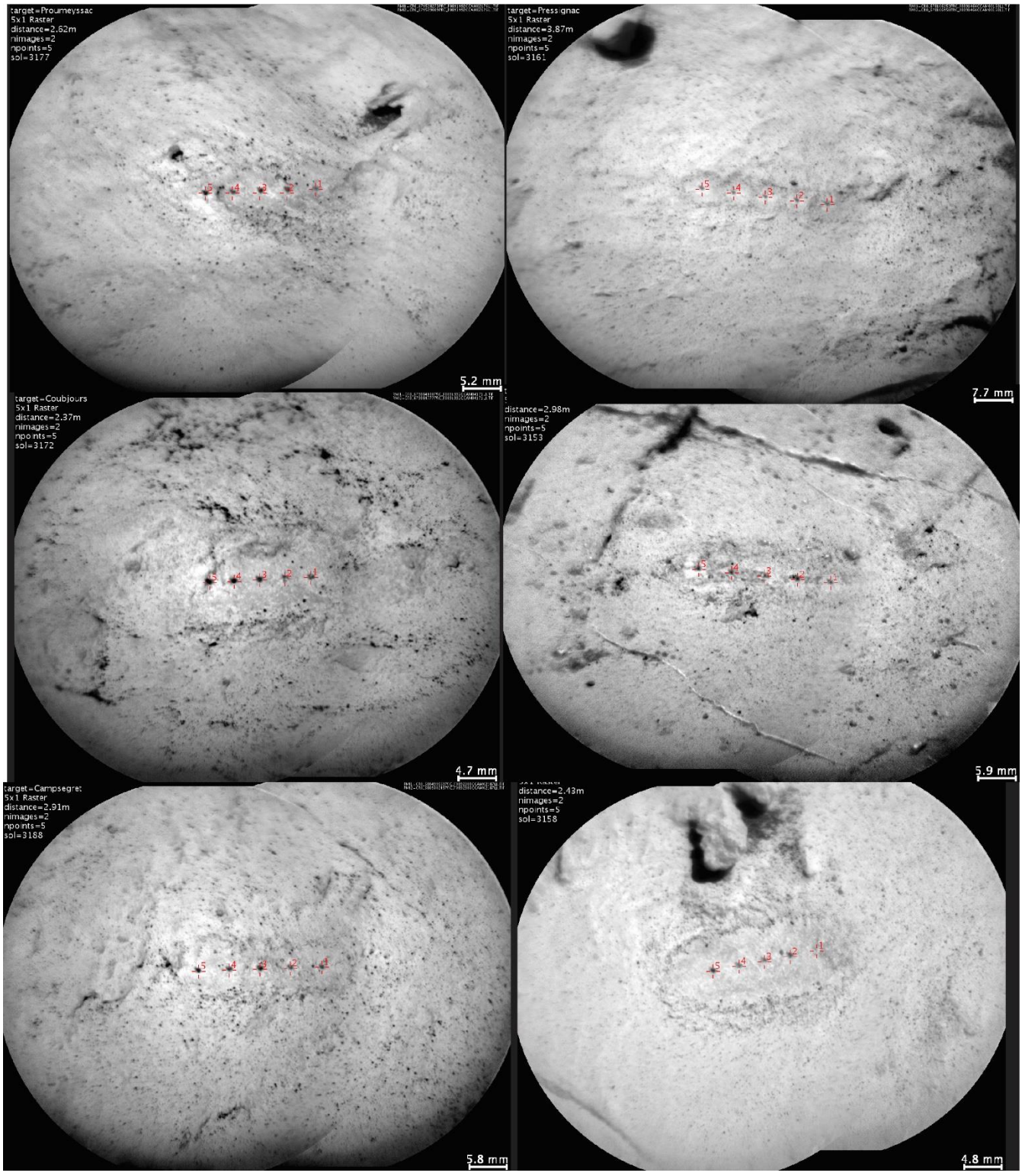

Extended Data Fig. 7: ChemCam images of fine-grained host bedrock. The bedrock matrix typically composed of a light-colored smooth-textured mudstone.

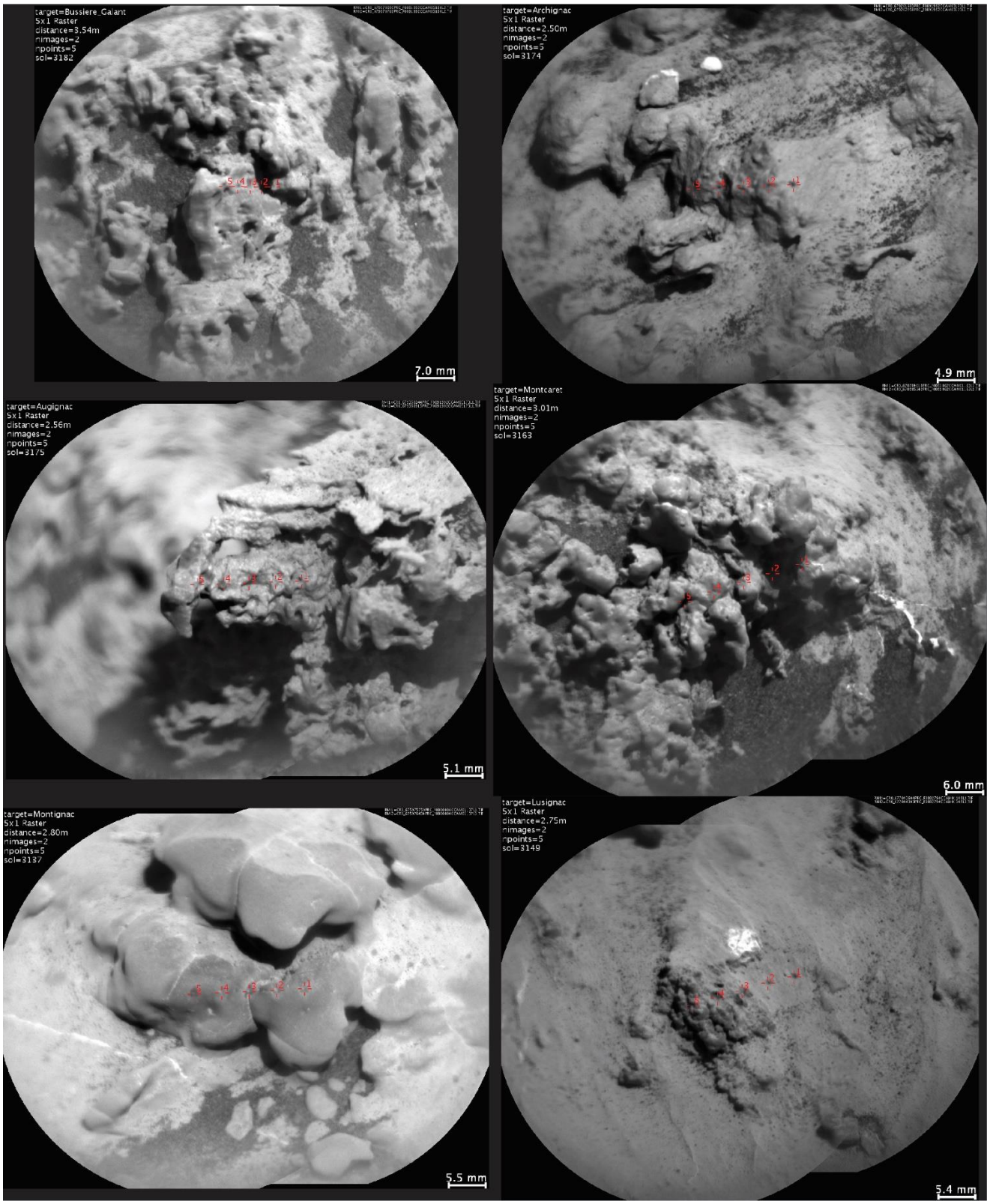

Extended Data Fig. 8: ChemCam images of nodular bedrock. Salt-bearing concretions are widespread and abundant in the examined section.

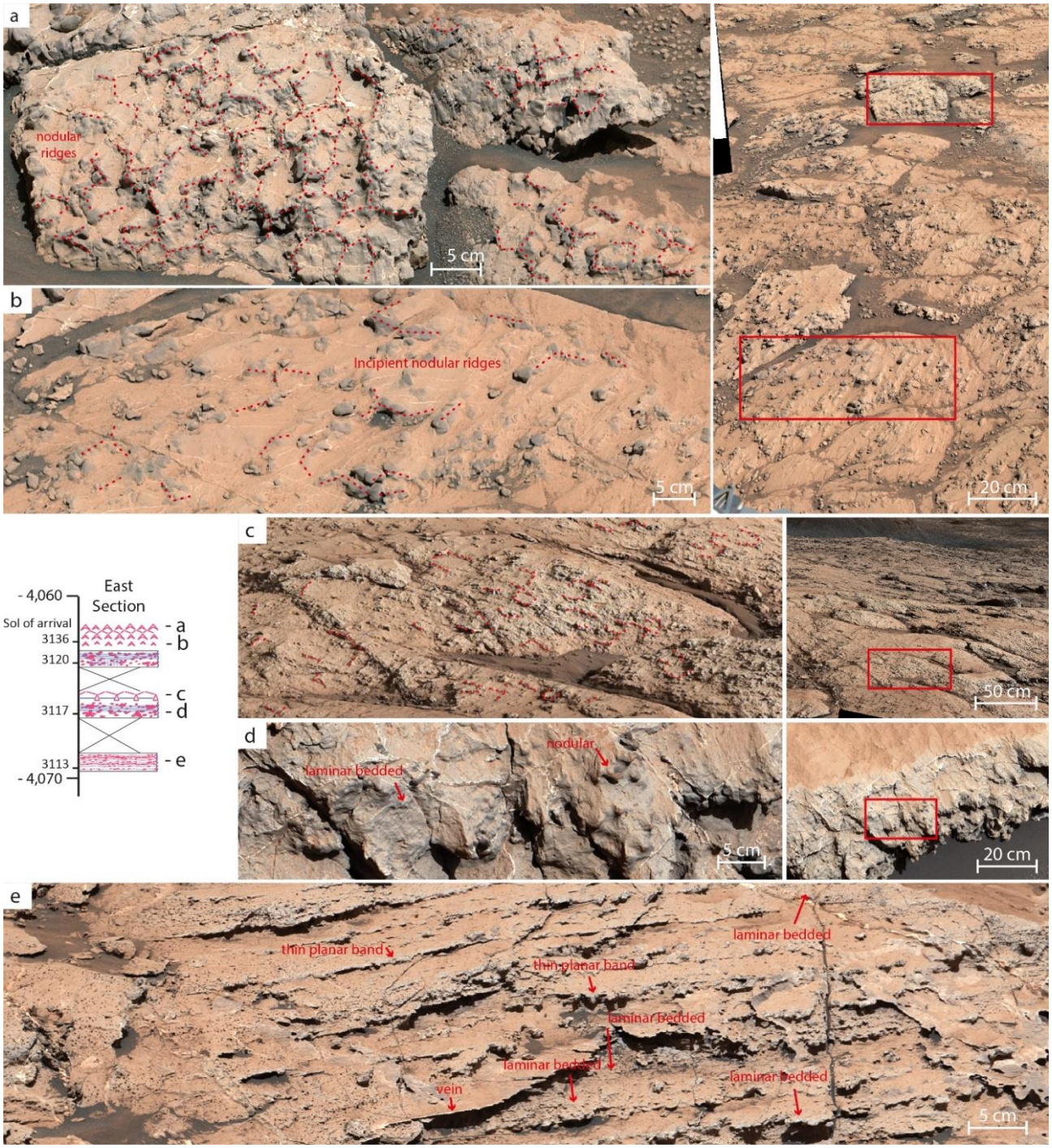

Extended Data Fig. 9: Stratigraphic log of East section. Lumped nodules organized in polygonal ridges (dotted lines) on bedrock block (**a**, sol 3137 Montaut). Lumped nodules forming possible incipient ridges (dotted lines) on bedrock (**b**, sol 3137 Montignac). Irregular nodules forming possible incipient or altered ridges (dotted lines) observed within nodular bedrock (**c**, sol 3117 drive_direction). Laminated bedrock with variably coalescent nodular texture (**d**, sol 3119 allas_les_mines). Aligned, variably coalescent micro-nodules within laminar bedded facies (**e**, sol 3112 garreloup).

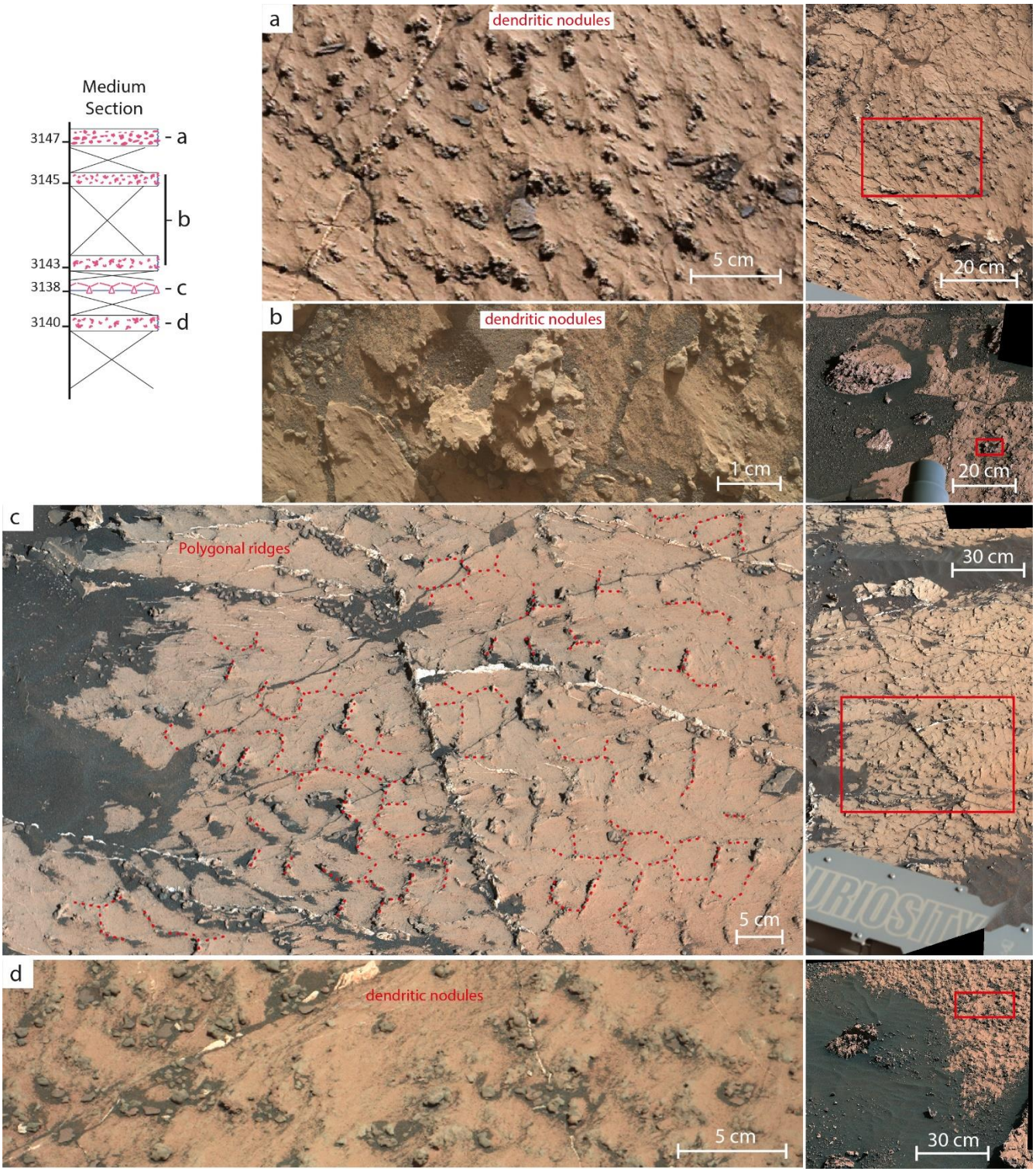

Extended Data Fig. 10: Stratigraphic log of Medium section. Bedrock with evenly distributed dendritic nodules (**a**, sol 3147 workspace). Close-up image of a dendritic nodule showing jagged, multifaceted, multi-centimeter texture (**b**, MAHLI target Nabirat 25 cm standoff). Incipient polygonal ridges (dotted lines) on bedrock (**c**, sol 3139 workspace). Dendritic nodules (**d**, MastCam on Vayres).

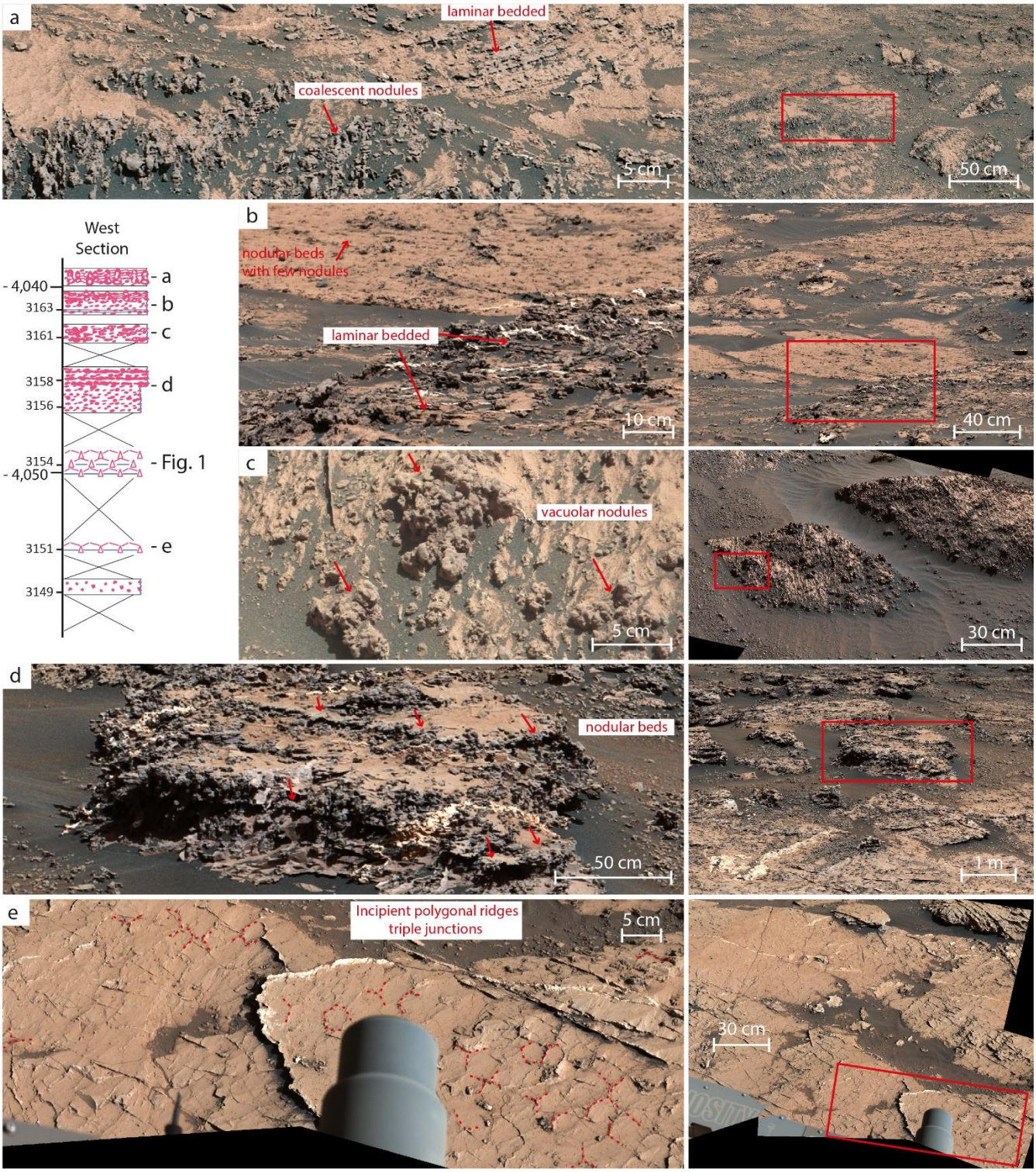

Extended Data Fig. 11: Stratigraphic log of West section. Partially coalescent nodules and laminar bedded facies (**a**, sol 3170 Organized_nodules). Nodular bedrock and laminar bedded facies adjascent to smooth or laminated bedrock at Pontours location (**b**, sol 3163 drill_area_context). Large, polymorphic vacuolar nodules (**c**, sol 3161 workspace). Coalescent nodules aligned in planar beds (**d**, sol 3158 diagenetic_transition). Incipient polygonal ridges (dotted lines) on bedrock (**e**, sol 3151 workspace).

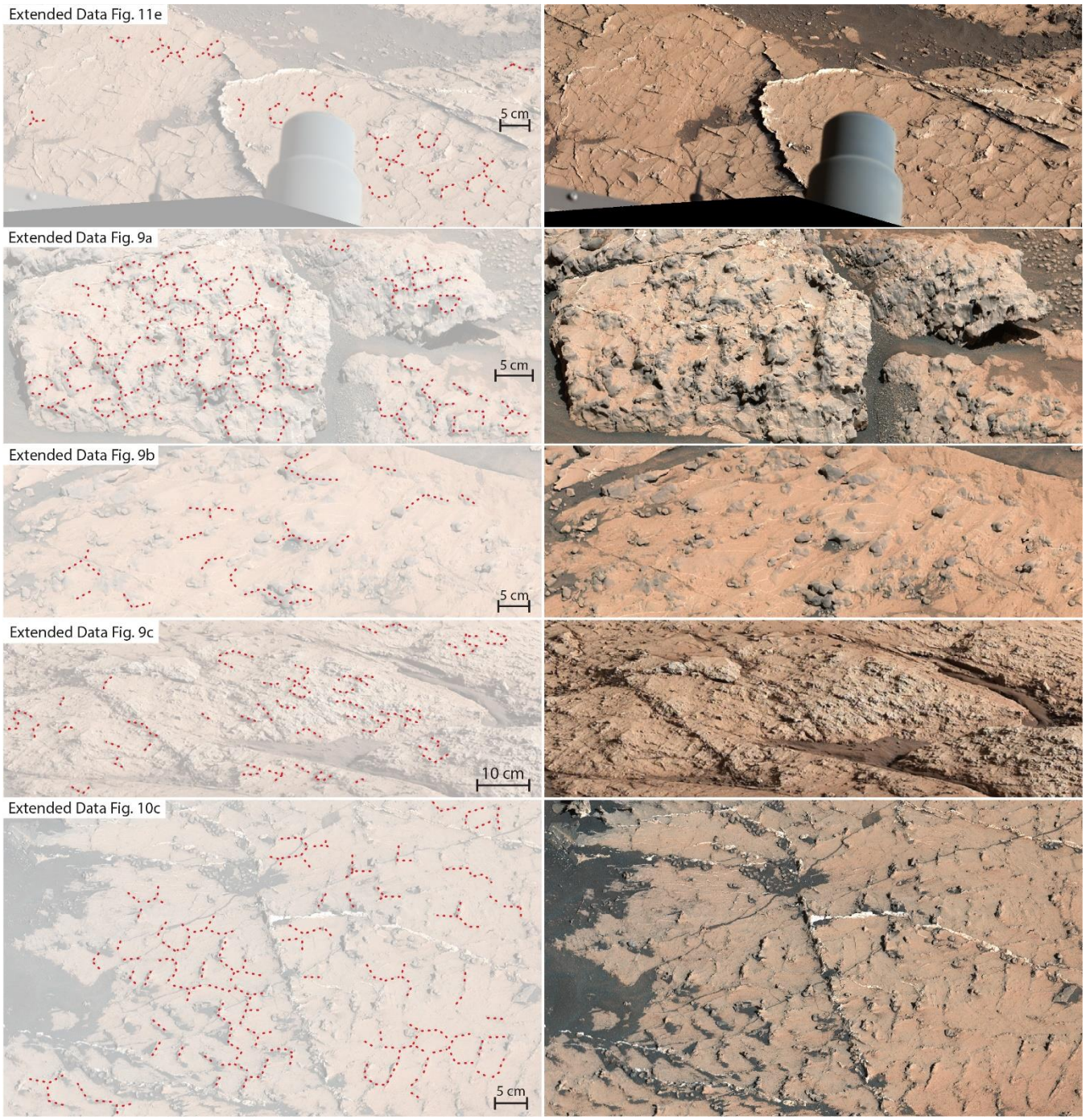

Extended Data Fig. 12: Polygonal pattern as incipient or altered variants. Details of images of other locations with possible polygonal ridges (dotted lines) from Extended Data Fig. 9-11 with markings (left) and without (right), see corresponding figures for context.

Supplementary information

Corresponding author contact information:
William Rapin
Chercheur CNRS
Institut de Recherche en Astrophysique et Planétologie (IRAP, UMR 5277)
Cell. +33769584256
Email william.rapin@irap.omp.eu

Contents :

Table S1: Statistical distribution of polygon sizes. Results on polygons size observed in each block (Extended Data Fig. 4). N = Number of measurements; SD = Standard Deviation. "Block 1 bis" is repeated Block 1 by a second operator.

	Sizes - Circle Diameters (cm)			
	Average	Median	Range	SD
Block 1 (N=168)	3.98	3.85	[1.82-6.93]	1.18
Block 1 bis (Op. 2) (N=176)	3.43	3.34	[1.30-6.70]	1.20
Block 2 (N=164)	3.98	3.89	[1.88-6.83]	1.07
Block 3 (N=145)	3.71	3.56	[1.73-7.56]	1.12
Blocks 1+2+3 (N=477)	3.90	3.76	[1.73-7.56]	111

Table S2: Chemical composition measured on polygonal ridges and other targets for context. Polygonal ridges (i.e. target Hautefort, Fig. 1d and Fig. 2) and incipient polygonal ridge (i.e. target Montignac, Extended Data Fig. 9b), as well average smooth host bedrock composition (avg. bedrock) from ChemCam data, along with APXS data from smooth host bedrock Ribagnac target (Fig. 1c). *APXS also reports compositional data for P2O5, MnO, Cr2O3, Cl, Ni, Zn and Br (see https://pds-geosciences.wustl.edu/msl/msl-m-apxs-4_5-rdr-v1/mslapx_1xxx/data/).

Target	SiO_2	+/-	TiO_2	+/-	Al_2O_3	+/-	FeO^T	+/-	MgO	+/-	CaO	+/-	Na_2O	+/-	K_2O	+/-	SO_3	+/-	H_2O	+/-
Hautefort #1	32.9	5.9	0.6	0.4	5.6	3.2	16.9	3.6	5.2	2.0	**11.3**	3.2	2.6	0.6	0.2	0.6	**21.0**	4.6	5.4	1.2
Hautefort #2	32.6	5.9	0.6	0.4	6.1	3.3	15.3	3.4	4.6	1.9	**14.4**	3.6	1.1	0.6	0.3	0.6	**22.9**	4.4	3.2	0.7
Hautefort #3	44.2	5.1	0.8	0.5	8.3	3.4	18.5	3.8	4.6	1.8	**8.9**	2.7	1.7	0.6	0.6	0.7	**7.1**	5.0	2.2	0.5
Hautefort #4	28.1	7.0	0.7	0.4	5.4	3.1	23.6	4.2	**10.5**	2.7	**8.0**	2.5	1.0	0.6	0.1	0.6	**19.8**	4.5	1.8	0.5
Hautefort #5	37.0	5.9	0.8	0.5	6.7	3.3	22.5	4.1	16.7	3.5	1.0	0.9	1.5	0.6	0.2	0.6	2.3	5.2	2.9	0.7
Montignac #1	41.5	5.0	0.9	0.5	8.3	3.5	18.4	3.9	**14.1**	3.3	1.3	1.0	1.7	0.6	0.6	0.7	**9.4**	5.1	3.5	0.8
Montignac #2	42.1	5.0	0.8	0.5	8.2	3.5	16.4	3.7	**14.8**	3.4	1.2	0.9	1.6	0.6	0.6	0.7	**10.0**	5.1	4.0	0.9
Montignac #3	39.1	5.1	0.8	0.5	8.0	3.5	17.6	3.9	**13.5**	3.3	3.0	1.3	1.4	0.6	0.3	0.6	**9.7**	5.0	6.0	1.3
Montignac #4	41.1	5.1	0.8	0.5	8.4	3.5	19.5	4.0	**10.7**	2.8	5.5	1.9	1.6	0.6	0.6	0.7	**8.9**	5.0	2.4	0.6
Montignac #5	40.8	5.1	0.8	0.5	7.8	3.4	19.4	4.0	**12.7**	3.1	2.9	1.2	1.5	0.6	0.5	0.7	**9.5**	5.0	3.5	0.8
Avg. bedrock	47.0		0.9		10.2		19.4		5.9		4.4		2.3		0.7		5.4		1.8	
APXS Ribagnac*	50.1	0.8	1.1	0.1	8.9	0.3	20.6	0.3	5.0	0.3	3.1	0.1	2.3	0.2	0.8	0.0	4.9	0.2	-	-

Table S3: List of ChemCam points in the examined section. Targets are classified as either host bedrock or nodular bedrock.

Host bedrock target	Sol	Point #
Monsec_ccam	3119	1, 2, 3, 4, 5
Millevaches	3122	1, 2
La_Donzelle	3124	1, 2, 3, 4, 5
Bourgnac	3126	1, 2, 3
Fossemagne_ccam	3136	1, 3, 4, 5
Lamourette	3139	1, 2, 3, 4, 5
Vayres	3142	1, 2, 3, 4
Sarlande	3145	1, 2, 3, 4, 5
Lacropte	3146	1, 2, 3, 4, 5
Lusignac	3149	1, 2
Biennac	3153	1, 2, 3, 4, 5
Barouffieres	3158	1, 2, 3, 4, 5
La_Lizonne	3160	3, 4, 5
Pressignac	3161	1, 2, 3, 4, 5
aegis_post_3164a	3164	4, 5
Chourgnac	3165	1, 2, 3, 4, 5
aegis_post_3166a	3166	1, 2, 3, 4, 5
Pontours_ccam	3167	1, 2, 3, 4
Dournazac	3169	1, 2, 3, 4
Coubjours	3172	1, 2, 3, 4, 5
Pontours_ccam_drill_hole_3173	3173	1, 2, 3, 4
Archignac	3174	1
Proumeyssac	3177	1, 2, 3, 4, 5
La_Bastide	3178	4, 5
La_Jemaye	3180	1, 2, 3, 4, 5
Ponteyraud	3181	2, 3

Nodular bedrock target	Sol	Point #
Millevaches	3122	3, 4, 5
Montignac	3137	1, 2, 3, 4, 5
Lusignac	3149	3, 4, 5
Salignac_Eyvigues	3151	1, 2, 3
La_Lizonne	3160	1, 2
Montcaret	3163	1, 3, 4, 5
Archignac	3174	2, 3, 4, 5
Augignac	3175	1, 2, 3, 4, 5
Berbiguieres	3176	1, 2, 3, 4, 5
Belcayre	3179	1, 2, 3, 4, 5
Ponteyraud	3181	4, 5
Bussiere_Galant	3182	1, 3, 4, 5